People's Democratic Republic of Algeria
Ministry of Higher Education and Scientific Research

University M'Hamed BOUGARA – Boumerdès

Institute of Electrical and Electronic Engineering
Department of Electronics

Project Report Presented in Partial Fulfilment of

the Requirements of the Degree of

'LICENCE'

In Electrical and Electronic Engineering

Title:

Solar Battery Monitoring System

Presented By:

- **Abayahia Hamou Zinedine**

Supervisor:

Pr. Abdelhakim Khouas

Registration Number:……../2022

Abstract

This study showcases a method of determining the health of solar panel batteries through the monitoring of voltage and current using microcontrollers. Most batteries have a limited useful life span which is further worsened when your system fails to comply with the battery manufacturer's given limitations; this leads to the need to prematurely replace your batteries, and therefore increase the total maintenance cost of your system. Existing solutions such as battery testers are expensive, inconvenient to use, and cannot adjusted for your specific needs. This project puts the emphasis on accurately monitoring the voltage and current using a microcontroller, in addition to estimating the charge level of the battery. In order to measure voltage and current as accurately as possible and deduce the state of charge, research about different types of analog to digital converters, current sensors, and state of charge (or battery percentage) algorithms has been done in order to determine the optimal design for such a task. Our design consists of using voltage dividers as attenuators in order to measure high voltages without damaging the analog to digital converters (ADCs) and placing the resistive current sensors on the low-side of the circuit. Tests were undertaken to check the performance of the aforementioned design. These tests revealed the superiority of resistor based sensors in regards of current sensing (achieving up to 0.72% accuracy), in addition, they proved that voltage can be obtained quite accurately and satisfy our system specifications (0.48% to 0.57% error).

Acknowledgements

Table of Contents

List of Figures

List of Tables

Abbreviations

General Introduction

With the recent spread of photovoltaic arrays in Algeria, certain measures need to be taken in order to maximize the useful lifespan of solar batteries, which are costly both for the buyer and for the environment. The aim of this project is to be able to determine battery voltage and current and then deduce the State Of Charge (SOC) for two 12V Lead-acid batteries in series; In order to achieve those goals, we propose a voltage and current acquisition scheme using ADCs with voltage dividers, in addition to resistive current sensors in the low-side of the load line. We also use Coulomb Counting and OCV techniques to deduce SOC. The data obtained (voltage, current, and SOC) will be uploaded to an online database for a quick and easy access. It is important to ensure proper data acquisition and processing for both current and voltage in order to deduce battery health and to estimate SOC as accurately as possible. Proper SOC determination will give us information about the overall energy consumption, while the voltage and current may be used to figure out a battery's age, vigor, and internal resistance.

The organization of this report is as follows. Chapter 1 introduces ADCs and their characteristics, in addition to voltage division. Different types of current sensor were also presented and discussed. The final section of chapter 1 puts the emphasis on SOC determination schemes and the phenomena that need to be taken into account for a decent estimation. Chapter 2 delves into the design specifications and the overall algorithm for obtaining the required data which is going to be implemented on the microcontroller. It also explains design choices for ADCs and the process by which we choose our ADC for the implementation. In addition, the necessity of having an active load in order to perform proper current accuracy testing has been emphasized before going into the details of current sensor choice. Chapter 3 contains a detailed overview of the implementation: it explains how the test circuits were constructed, and what conditions needed to be met for them to function properly. Chapter3 also contains a discussion of the results obtained through the previously mentioned tests and validates our system's reliability.

Chapter 1. Basic Concepts

1.1 Voltage Measurements

In order to measure analog voltages using a microcontroller, an analog to digital conversion needs to take place. Both Successive Approximation Register (SAR) and Delta-sigma analog to digital converters (ADCs) are suitable options for measuring voltages as long as they meet the Nyquist sampling criterion and have a sufficient resolution to reduce the quantization error [1]. For battery terminal voltage measurements, we theoretically do not need high sampling rates. Certain SAR ADCs do require an ample amount of oversampling and averaging in order to reduce the output's sensitivity to noise.

1.1.1 ADC Characteristics

1.1.1.1 ADC Definition and Function
ADCs are systems that convert various analog signals into discreet signals that a microcontroller can process. While most microcontrollers do have integrated ADCs, you can attach an external ADC if the specifications of the integrated ADCs are not suitable for your application.

1.1.1.2 ADC Noise
 ADC noise is composed of input voltage noise in addition to quantization noise resulting from the uncertainty of the measurement (the analog signal having an unlimited number of digits while the digitized quantity only has a limited number of digits [1]). We have to take ADC noise sensitivity into account when choosing our ADC. We can quantify this noise using the signal to noise ratio formula.

$$SNR = \frac{Vsignal(RMS)}{Vnoise(RMS)} \tag{1.2.2}$$

Alternatively, we can plot the graphs for output voltage variations and compare their noise peaks.

1.1.1.3 ADC Linearity

ADC linearity is the Root-Mean-Square difference between true linear response and actual readout [2]. It represent the degree of tilt compared the linear response (input equals output) and can be seen graphically.

Chapter 1. Basic Concepts

1.1.2 Oversampling and Averaging

Oversampling and averaging (OVS) (also called Multisampling [3]) is a common technique used to mitigate the effect of noise on the output. Oversampling is done by sampling the original signal many times more than the required sampling frequency as per the Nyquist Theorem.   The aforementioned samples are then stored, summed, and then divided by the total number of samples acquired [4].Figure 1.1-1, Figure 1.1-2, and Figure 1.1-3 show how different averaging factors affect the noise sensitivity of the ADC. Two-Hundred serial samples were plotted for each oversampling factor using the Arduino IDE's serial plotter. The y-axis represents the ADC output in digits (meaning in decimal) while the x-axis represents the number of samples taken. The serial plotter adjusts the scale of the image according to the magnitude of the y-axis; therefore, it is important to only take the numbers into account, not the size of the graph. **We will be referring to the decimal output of the ADC as ADC output (in digits) for the rest of the document**.
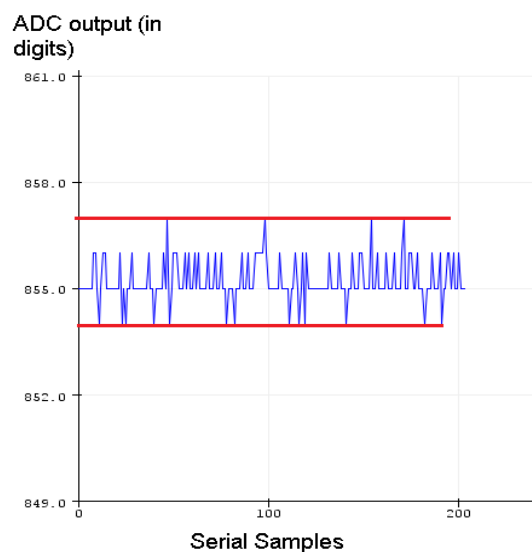
Figure 1.1-1 : ADC readings with multisampling factor 64.
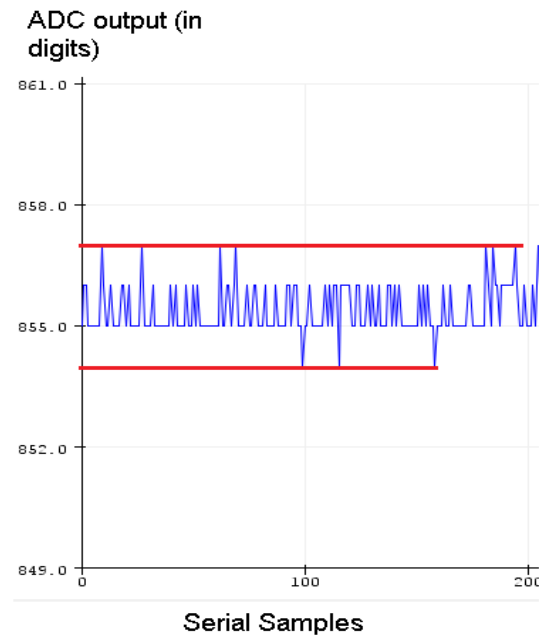
Figure 1.1-2 : ADC readings with multisampling factor 128.
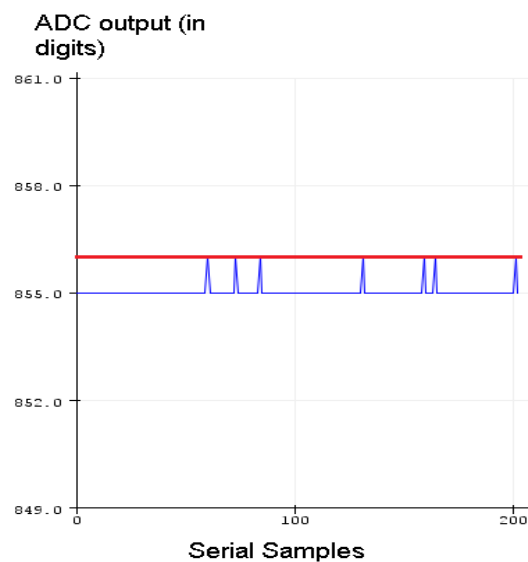
Figure 1.1-3 : ADC readings with multisampling factor 1024.

The red lines represent both the maximum and minimum value for the noise. We can notice that the bigger the oversampling factor, the more certainty we can achieve about the signal (less peaks and disturbances are apparent; see Figure 1.1-1 and Figure 1.1-2). If we

4

increase the oversampling factor even further, we can almost nullify the noise as shown in Figure 1.1-3.

One disadvantage of this technique is the reduction of the effective sampling rate. Since we are taking multiple samples of the signal before getting any information, we are reducing the true sampling rate of our ADC by a factor equal to the number of taken samples. In order to counter act this, we will have to further increase our sample rate.

1.1.3 Reference Voltage Calibration

Reference voltage calibration is the process by which we eliminate (compensate) for the drift in the external reference voltage of the ADC. This operation can be done through measuring the internal reference (also called the "bandgap") by routing this reference voltage through the use of internal circuitry and calibrating accordingly. A high accuracy external source can also be used for a better estimation of the bandgap and a better overall accuracy [5]. The ESP32 module's ADCs only have a single internal reference voltage (independent of the supply rails). Their calibration process can be achieved manually through routing to a general purpose input output pin (GPIO) before reading the voltage with a multi-meter, or automatically, by reading the internal e-fuse directly [3].

1.1.4 Quantization Error

Quantization error is the uncertainty in measurement caused by the inability of limited ADC resolution bits to represent an analog signal containing infinite digits after the decimal point. We use the following equation to obtain quantization noise for a given ADC:

$$Err = \pm \frac{RES}{2}$$
(2.3.6)

Where Err is the quantization error and RES is the resolution given by:

$$RES = \frac{Vref}{2^{bits} - 1}$$
(3.3.6)

Vref is the ADC reference voltage and *bits* is the number of resolution bits.

1.1.5 Voltage Dividers

Voltage dividers are used to attenuate the measured signal's amplitude to safer levels for the GPIOs of the microcontroller. We can also use them to bias our input signal into the desired area of measurement in order to increase accuracy (will be explained later).

Chapter 1. Basic Concepts

1.2 Current Measurements

There is a wide variety of modern techniques that allow us to accurately measure current. These methods are often based on Ohm's law, the Hall effect or Faraday's law; all of which produce reliable results under different circumstances [6].

1.2.1 Resistive Sensors

Resistive sensors use Ohm's law to measure current: a shunt resistor (sense resistor) is often placed in series with the load before measuring its voltage drop using an ADC. We then use Ohm's law to deduce the current from the obtained voltage.

$$I = \frac{Vain}{Rsense} \qquad (4.1.2)$$

These sensors generally use a differential amplifier or a PGA (Programmable Gain Amplifier) to eliminate the common mode noise and to avoid loading the resistor nodes. They are generally more accurate than other types of sensors. Figure 1.2-1 is the simplest existing topology for a current sensor.
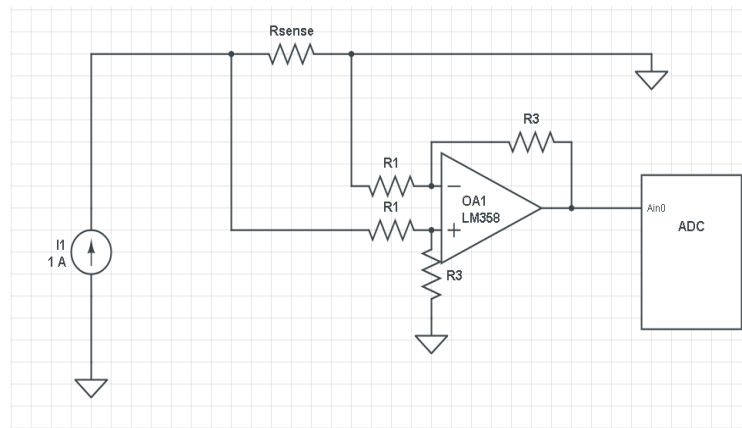
Figure 1.2-1 : Simple current sensing circuit.

1.2.2 Hall Effect Sensors

These sensors are based off of the Hall effect which was discovered by Edwin Hall in 1879. He found that when a current flows through a thin sheet of conductive material that is penetrated by a magnetic flux density, a voltage is generated perpendicular to both the current and field. The conductive material is often called a Hall element and cannot be used to accurately measure the current on its own. The magnetic flux from the current that we want to measure must be perpendicular to the sheet, in order to achieve that, a magnetic core, or a current carrying conductor (to be discussed later) is used to drive the magnetic flux straight into the Hall element as shown in Figure 1.2-2.
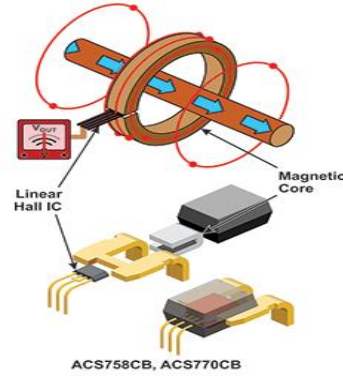
Figure 1.2-2 : Hall effect sensor [7].

1.2.3 Current Transformers

Current transformers (CTs) are sensors that measure current using Faraday's law of induction:

$$v = -N\frac{d\varphi}{dt} \qquad (5.1.2)$$

Where N is the number of turns, φ is the magnetic flux, and v is the generated voltage. Some CTs are "DC capable" which means that they are able to measure DC currents as well as low frequency AC currents. Closed loop (compensated) current transducers using the Hall effect are a type of DC capable CTs. As shown in Figure 1.2-3, the primary current Ip flows through the wire, and a magnetic flux is generated through the core. The Hall effect sensor detects the magnetic field and generates a voltage which is then amplified to drive a current through the secondary winding (the wound coil). In return, this current creates a flux which opposes the flux due to the primary and nullifies it. In doing so, we obtain an attenuated replica of the primary current in the secondary winding (Is) flowing through RS [8]. This is why this type of CT is sometimes referred to as the Zero-Flux CT [9]. The main advantage of such a design is the ability to measure currents with both an AC and DC component without saturating the core. This allows us to measure AC, DC, and varying DC currents with a very high accuracy.
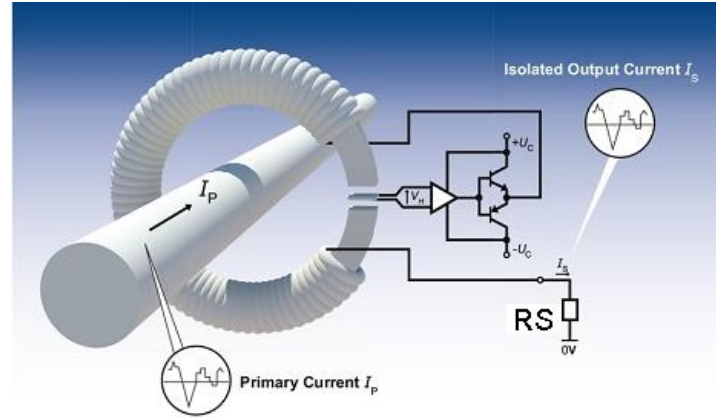
Figure 1.2-3 : Compensated current transducer using the Hall effect [8].

1.3 SOC Determination

SOC is the level of charge of an electric battery relative to its capacity. Its unit is percentage points or ampere-hours depending on the application. Determining the SOC of any battery type can be quite a challenging task: even certain commercial products such as phones and laptops fail to correctly estimate the remaining charge in a battery. The myriad of factors that influence battery behavior are to blame for those failures. The most notable factors that influence battery behavior are -in order of importance- the rate of discharge, temperature, battery age, the charging efficiency electrochemical balance, and the self discharge current. Empirical methods are employed to model battery behavior mathematically; these methods are reliable for battery percentage estimation regardless of their shortcomings compared to the more complex chemical and thermodynamic based methods. We will mainly be focusing on translation and book-keeping methods in this study [10].

1.3.1 OCV Method

OCV method consists of accurately obtaining battery voltage and then **mapping** the remaining capacity from it according to a known OCV to SOC graph which is also called the discharge curve [10] (see Figure 1.3-1).

Chapter 1. Basic Concepts
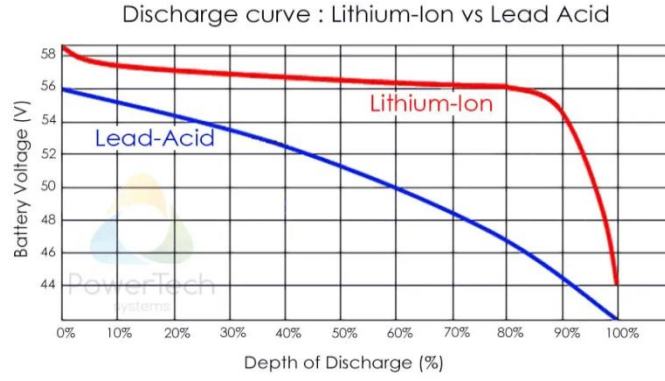
Figure 1.3-1 : Typical discharge curves for Li-Ion and Lead-acid batteries [11].

This method –on its own- cannot be used for determining the SOC in our application. Battery terminal voltage does not equate open circuit voltage. Since all batteries have internal resistances, discharging these batteries at high currents will cause a voltage drop between the terminal voltage and the battery itself [12]. Furthermore, the battery's open circuit voltage can only be used as an indicator for battery SOC if the battery has reached electrochemical balance; for that to happen, the battery needs to be disconnected from the load and left to rest for about two hours before taking the voltage measurements [10]. For photovoltaic system batteries which are used to supply house appliance, that would not be feasible. That aside, certain battery types such as Li-ion batteries have very flat discharge curves as seen in Figure 1.3-1. This makes it very hard to map the remaining capacity directly from the graph.

1.3.2 Coulomb Counting

Coulomb counting is the process of obtaining the number of remaining charges in a battery through the continuous integration of current [13]. It is one of the most wide spread book-keeping methods for SOC estimation. Equation 6.1.3 is the mathematical definition of coulomb counting.

$$SOC(t) = SOC(t_0) + \int \frac{\eta(T,SOC,I,Ic)I(t)}{Ca} \, dt \qquad (6.1.3)$$

Where T is the temperature, Ic is the charging current, I is the discharge current before the charging process, SOC is the charge level, $\eta(T,SOC,I,Ic)$ is the coulombic efficiency, which is set to 1 during discharge (not present during discharge), Ca the actual capacity of the battery (replaced by Cn the nominal capacity during the charge process), and I(t) the current flowing through the battery. Coulomb counting is also called Enhanced Coulomb

Chapter 1. Basic Concepts

Counting when it accounts for temperature and the Peukert effect which will also be discussed later. The main issue with coulomb counting is the need to have an accurate estimate of the initial value of the SOC ($SOC(t_0)$), in addition to the drift caused by the accumulation of integration error. Accurate current measurements are also required to insure a good overall accuracy.

1.3.3 Coulomb Counting with OCV Calibration

Combining the two previous methods yields a robust algorithm that is does not have the previously discussed issues [10]. First, we obtain the initial SOC of the battery through disconnecting the battery for about two hours before powering our circuit. The circuit will automatically measure the terminal voltage and map the initial SOC from the discharge curve. It is important to note that this process can only be applied to lead-acid batteries which have an approximately linear discharge curve. As can be seen in Figure 1.3-2, Li-Ion batteries seem to have very flat discharge curves in the middle range from 90% to 10% depth of discharge (DOD); beyond that however, the curve has a significant slope. We can obtain the initial SOC from there provided that the battery has been charging for a very long period of time. Coincidentally, the regions outside the middle of the graph (100% to 90% and 10% to 0%) are characterized by low charge flow (almost full or almost empty battery) which allows us to estimate the SOC around those regions through the terminal voltage relatively well [14]. We can set the integral to zero and map $SOC(t_0)$ from the discharge curve at those regions in order to calibrate the integral and avoid cumulative error. This process can be applied to both battery types. Lead-acid batteries allow for the possibility of multiple point calibration because of their linear curves. This algorithm does not take into account battery age and battery temperature; it works best for lead-acid batteries.
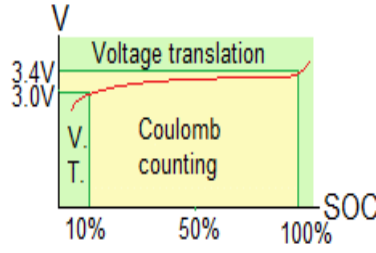
Figure 1.3-2 : Coulomb counting and OCV method for SOC estimation [14].

1.3.4 Peukert Effect

A battery's nominal capacity is often determined in a laboratory setting under a set of very specific conditions. Most battery manufacturers test their batteries at a discharge rate of C/20 (also called the 20 hour rate, which implies discharging the battery at a current that will fully discharge the battery in 20 whole hours [15]). In reality, battery capacity shrinks whenever the discharge rate increases; this is one of the many reasons why many engineers do not trust the nominal capacity rating for determining battery capacity. This effect is called the Peukert effect; it occurs partially due to the sudden voltage drop which brings the battery current flow to a trickle (low current discharge) [15]. The other prominent causes for this effect are electrolyte movement and internal resistance changes [16]. This effect can only be modeled empirically and not physically in the case of electrical SOC determination; that is due to its complexity and its dependence on various factors. The current drawn out of the battery is then set to the nth power to model this effect. this exponent (n) is referred to as the Peukert exponent (usually denoted pc or n) and varies between 1 and 1.5 depending on the battery. It expresses the shrinking capacity with the increase of the discharge rate (high currents discharge the battery faster) [16].

$$Cp = I^{pc} \cdot t \tag{7.1.3}$$

Cp is the peukert capacity which is constant no matter the discharge rate for a single battery (not analogous to the actual capacity), I is the actual discharge rate in Amps, and t is the duration of discharge in hours.

This, in turn, gives us 8.1.3.

$$Ca = \frac{Cn(In)^{pc-1}}{I^{pc}} \tag{8.1.3}$$

Chapter 1. Basic Concepts

Alternatively, we can define an effective current I_{eff} which we integrate directly to get the change in SOC as follows:

$$Ieff = \frac{I}{Ca} \tag{9.1.3}$$

$$SOC = SOC(t_0) + \Delta SOC \tag{10.1.3}$$

$$\Delta SOC = \int Ieff\ dt \tag{111.3}$$

Before implementing the algorithm however, we would need to first determine the Peukert exponent. In order to do so, the batteries need to be discharged at two different discharge rates. The first one (denoted I_1) is taken as a reference and should be as close as possible to the average current I_{avg} flowing through the battery when it is being loaded by house appliances. The second discharge rate I_2 should be much lower in order to linearly sweep all possible discharge rates, in addition to being able to neglect the change in the Peukert exponent due to battery imperfections [17].

Since Cp is the same for all discharge rates, let's define Cp1 and Cp2 such that:

$$Cp1 = Cp2 \tag{12.1.3}$$

From 7.1.3 we get:

$$C1(\frac{C1}{t1})^{pc} = C2(\frac{C2}{t2})^{pc} \tag{13.1.3}$$

Where C1 and C2 are the available capacities at the discharge rates I1, and I2 respectively, and t1, t2 are the obtained discharge durations after the discharge tests. We solve for pc and find:

$$pc = \frac{\log(t2) - \log(t1)}{\log(I1) - \log(I2)} \tag{14.1.3}$$

It Is important to note that bigger Peukert exponents increase the capacity's dependence on the discharge rate and make this effect more pronounced.

1.3.5 Self-Discharge

Self-discharge current is the constant internal current draw inside the battery due to its chemical reactions: it is the energy loss of the battery.

Chapter 1. Basic Concepts
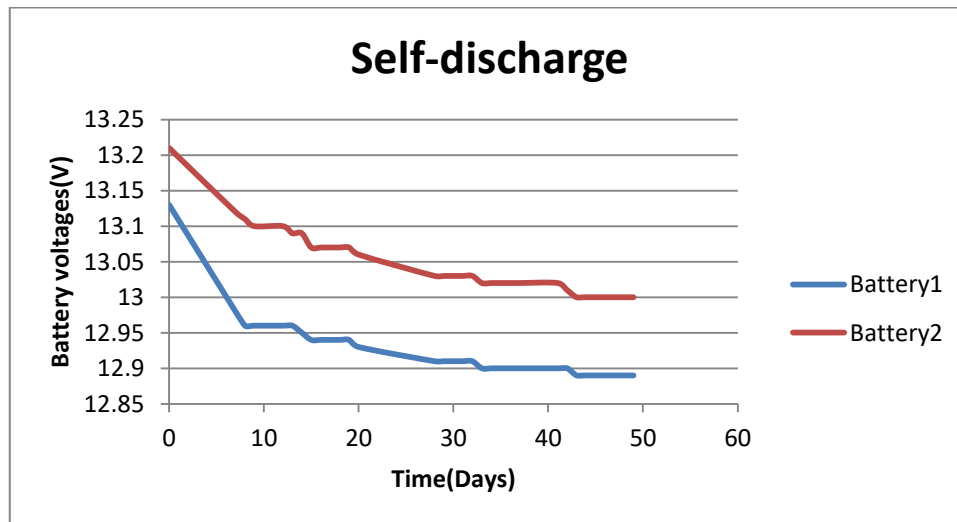
Figure 1.3-3 : Self-discharge curves of two Lead-acid batteries.

Figure 1.3-3 shows a plot of the battery voltages to the number of days after initial charge (battery voltage measurements were taken once every three days for 49 days. Current was not drawn out of the batteries during that period of time. These graphs are also called battery charge retention curves, and the voltages can be replaced with their corresponding SOC since the batteries are electrochemically balanced. We can clearly see an exponential characteristic which is common for Lead-Acid batteries.

Self-discharge is an important factor in determining coulombic efficiency (will be discussed later) at low discharge rates. Knowing the self-discharge current also allows us to use Peukert's law for all discharge rates (including when no current is being drawn out of the battery) since the current is never –truly- zero and therefore the actual capacity (Ca) will never go to infinity (see equation 8.1.3) [16].

1.3.6 Coulombic Efficiency

The charging efficiency represents the amount of charges we can extract from a battery relative to the amount of charges that we put into the battery during the charging process. Mathematically speaking, it is the ratio of the number of charges taken out of the battery to the number of charges available [15]. Determining the coulombic efficiency of a given battery is a tedious task that requires a lot of testing. charge efficiency is affected by a multitude of factors such as: the rate of discharge, temperature, the present time SOC of the battery, the charging rate of the battery, in addition to the self-discharge current when it

is non negligible compared to the current draw [15] [12]. Obtaining the charging efficiency coefficient is done through extensive discharge and charge tests on the battery under different temperatures. Charge efficiency determination is outside the scope of this project report.

Chapter 2.   Solar Battery Monitoring Design

2.1 Specifications

The batteries that were used for the testing voltage accuracy are two 12V Lead-acid batteries having a rated capacity of 7Ah and 9Ah. The solar batteries we want to monitor are two 12V batteries in series which can have currents up to 50A drawn out of them. All exact values for voltage and current measurements were obtained using an ANENG8009 multi-meter with a ± 1% voltage error and a ± 2% current measurement error. Voltage and current measurements with a maximal error of 3% and 2% respectively are required for our design to meet.

2.1.1.1 Microcontroller and Cloud Choice

Since we need to upload the data to an online cloud, Espressif systems' ESP32-WROOM was chosen as the main microcontroller of our system. This module is a Dual-core microcontroller with a reliable Wi-Fi peripheral. Thingspeak is an online database that allows for data plotting in real-time and for automatic time storage. This makes it ideal for our project. The Thingspeak IDF library was used in order to send the data from our microcontroller to the cloud storage.

2.2 Voltage measurements

While trying to devise the best circuit design for voltage measurements, I have encountered a few issues that needed to be dealt with; mostly related to ADC characteristics and wiring; therefore, ADC choice, wire gauge and wire placement are of the utmost importance. For this project, we will consider three options for measuring voltage: the ESP-WROOM-32's internal ADCs, the ADS1115 Delta-sigma external ADC with I2C communication, and the STM32F303RET6 NUCLEO's internal ADCs. The STM32 microcontrollers are known for having very reliable ADCs; this model in particular has an ADC capable of reaching sampling rates of up to 5Mhz. This is why they were considered for this project. The chapters below are a comparative study based on multiple tests done on these pieces of hardware. Before performing any measurements, we need to first get the reference voltage from the efuse of the ESP32 ADC through a python script provided by Espressif ESP-IDF called espefuse.py (see Figure 2.2-1).

Chapter 2. Solar Battery Monitoring Design

```
Connecting....
Detecting chip type... Unsupported detection protocol, switching and trying again...
Connecting....
Detecting chip type... ESP32
espefuse.py v3.2
ADC VRef calibration: 1086mV
```

Figure 2.2-1 : Reading Vref from the efuse.

2.2.1 Noise Tolerance Comparison

In order to learn more about the robustness to noise of our ADCs, we compare the noise graphs of the ESP32 ADCs, the ADS1115 at a full-scale range (FSR[1]) of 6.144V, and the STM32 NUCLEO. As mentioned earlier in section 1.1.2, the Arduino IDE was used to plot 200 serial samples where the x-axis is the number of the serial samples and the y-axis is the ADC output in digits (meaning the ADC output bits were converted into decimal and shown as output) . The graphs are scaled down depending on the amplitude; therefore only take numbers into account when analyzing them and not the size of the graph. The figures below were obtained.
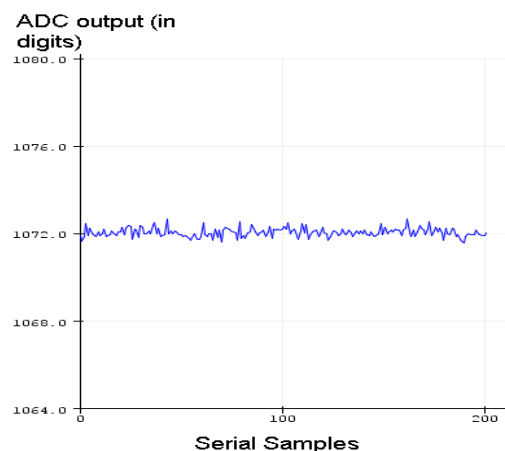
Figure 2.2-2 : Noise graph of the ESP32 ADC OVS 1024.

---

[1] At FSR 6.144V the ADS1115 has the best noise tolerance according to its datasheet.
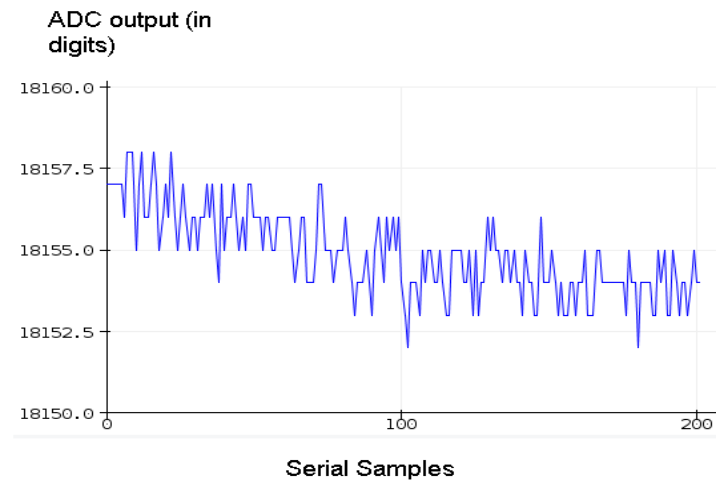
Figure 2.2-3 : Noise graph of the ADS1115 at sampling frequency 128hz at FSR 6.144V.
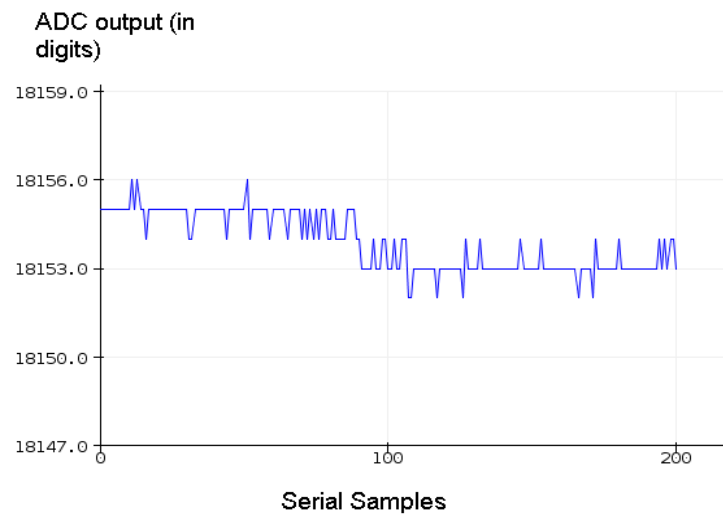
Figure 2.2-4 : Noise graph of the ADS1115 at sampling frequency 32hz at FSR 6.144V.
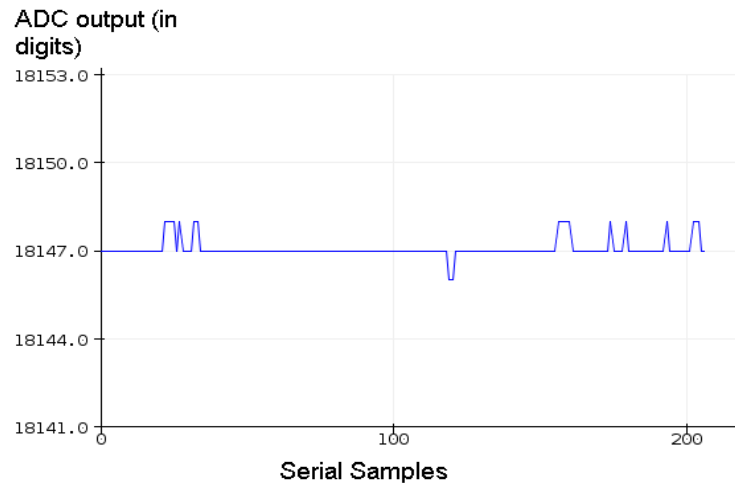
Figure 2.2-5: Noise graph of the ADS1115 at sampling frequency 8hz at FSR 6.144V.

Since the ADS1115 is a Delta-Sigma ADC, it already incorporates oversampling and averaging through its hardware, more specifically, its integrator; therefore, whenever we decrease its sampling rate, we are actually decreasing its effective sampling rate only and not its internal clock frequency. That means that every time we decrease the sampling frequency, we are actually increasing the oversampling factor, which is why the signal is less sensitive to noise at lower sampling frequencies. This can be seen in the figures above.
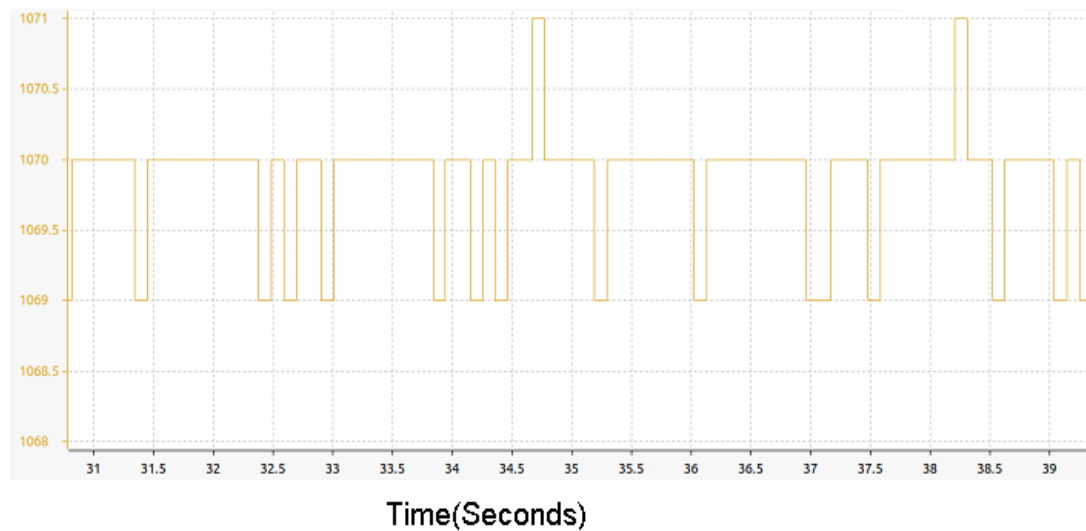
Figure 2.2-6 : Noise graph of the STM32NUCLEO at a sampling frequency of 5Mhz at OVS 10^2.

The STM32's ADC has a surprisingly good noise tolerance at such a high sampling frequency, even beating a dedicated external ADC such as the ADS1115 at its lowest sampling frequency.

2.2.2 ADC Linearity Comparison

In order to view ADC nonlinearity, we used a potentiometer to sweep all the input range of the ADC and recorded those values at an interval of 100 mV (after measuring the real voltage using the multi-meter) and plotted them. The x-axis represents the real voltages in V and the y-axis represents the ADC output in V. The red line represents an ideal, perfectly linear ADC.

---

[2] The STM32's graph was plotted using the STM32CubeIDE Serial Wire Viewer.

ESP32 ADC Linearity (no mapping)

Figure showing ADC Output (V) vs Real Voltages (V), with two curves: ESP32 ADC (no mapping) in blue and Ideal ADC in red.
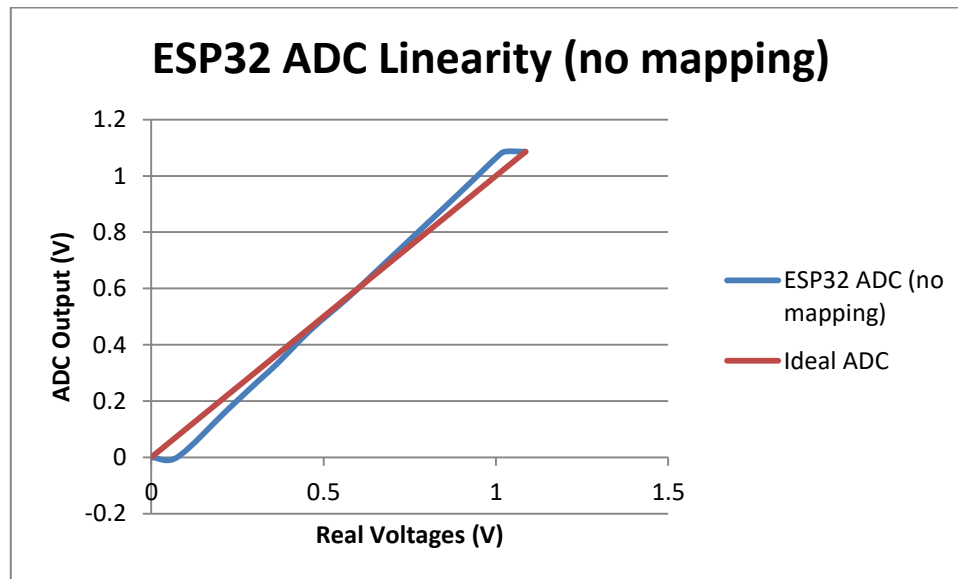
Figure 2.2-7 : ESP32 ADC output curve (no mapping).

We can see that the ESP32's ADC behavior is highly non-linear in Figure 2.2-7, especially towards the start and the end of its measurement range. In order to counteract this, Espressif has added a software compensation application programming interface (API) called esp_adc_cal which plots the ADC characteristic curves and saves data so that it can map the corrected output voltages from it.

ESP32 ADC linearity (with mapping)

Figure showing ADC Output(V) vs Real voltage (V), with two curves: ESP32 ADC (mapping) in blue and Ideal ADC in red.
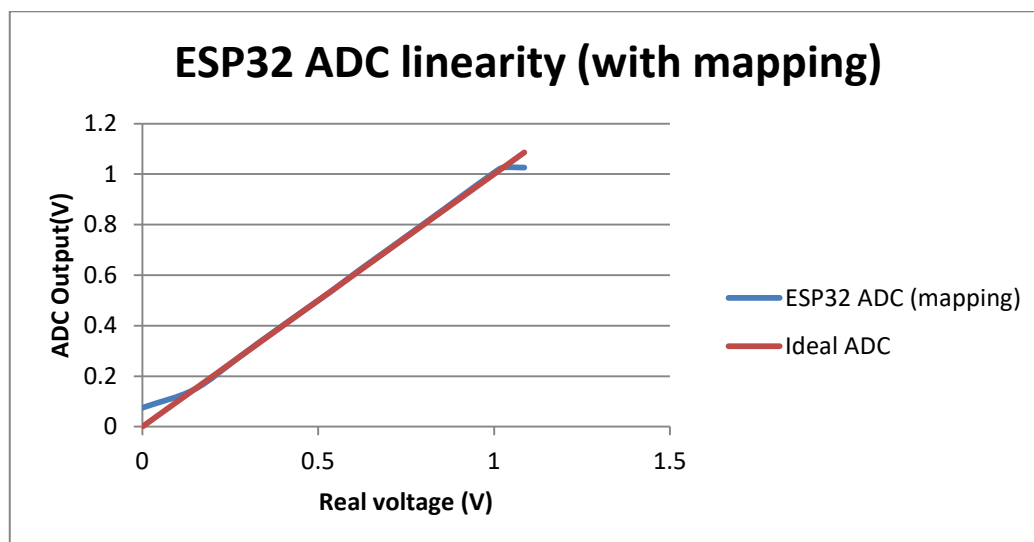
Figure 2.2-8 : ESP32 ADC output curve (with mapping).

As we can see in Figure 2.2-2, the API adjustment makes the output characteristic perfectly linear at the middle range of the ADC.

ads1115 Linearity(FS=6.144, 8sps)
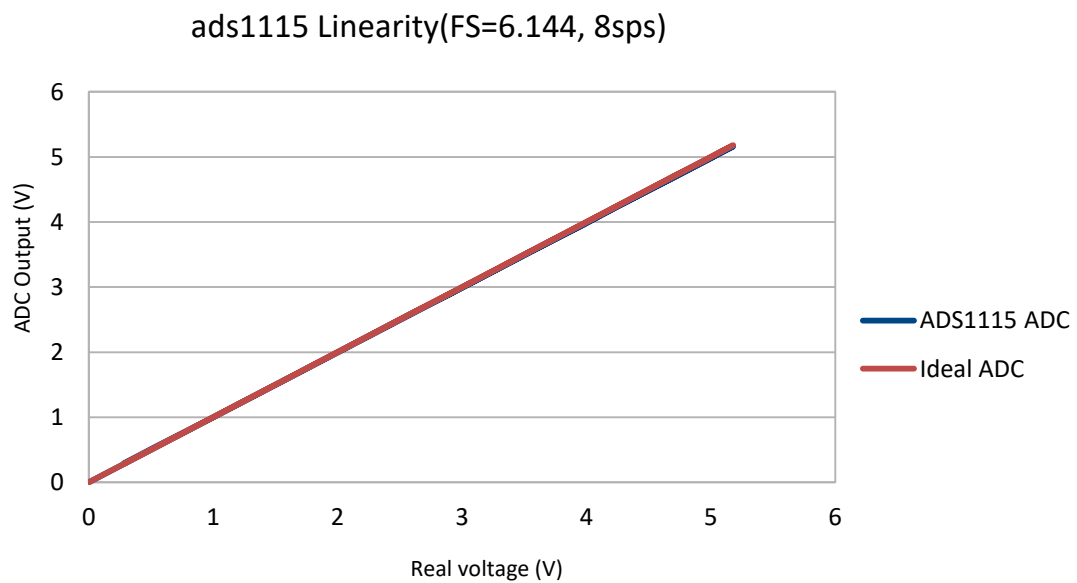
Figure 2.2-9 : ADS115 linearity.

Linearity of the STM32 ADCs
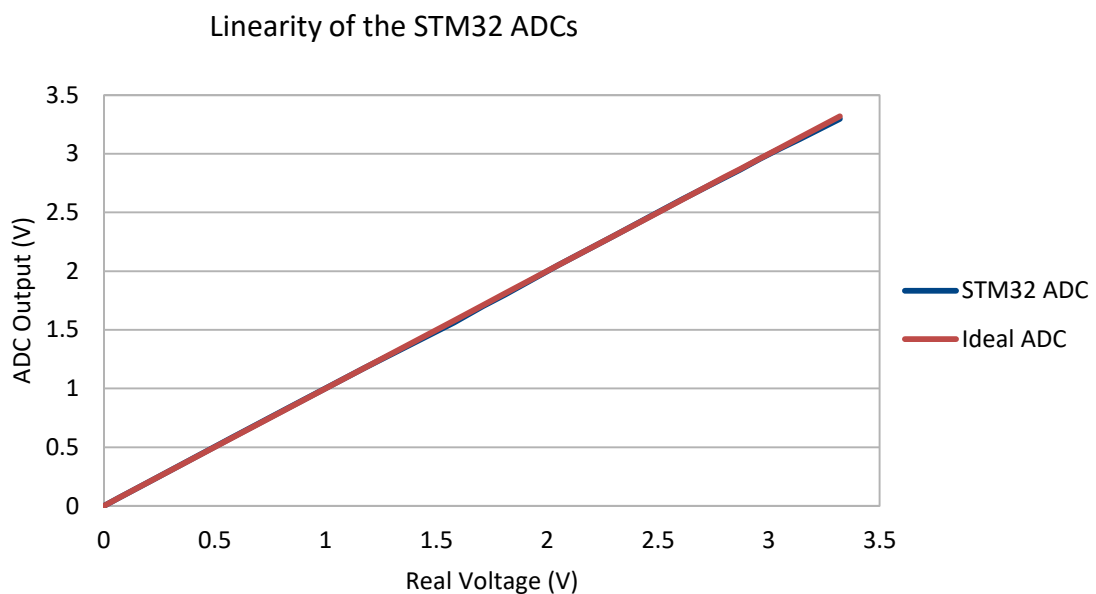
Figure 2.2-10 :STM32 ADC linearity.

Both the ADS1115 and the STM32NUCLEO ADCs have a linear behavior throughout their complete range of measurement (see Figure 2.2-9 and Figure 2.2-10).

2.2.3 Comparing the ADCs

A few more aspects need to be studied before choosing our ADC. For instance, the ADS1115 is a 15 bits (an additional bit is dedicated for polarity) ADC unlike the

aforementioned options. In addition, it offers bidirectional measurements (it allows us to measure negative voltages), as long as we do not violate its common mode limits (V_{supply}+0.3 >Vin> GND-0.3). This can be extremely useful for current sensing.

The STM32NUCLEO is the most expensive option and needs to have a method of communicating the results of the ADC conversions to the ESP32 without damping the sampling frequency. This can be quite complicated. The ESP32's internal ADCs are simplest, cheapest, and most convenient option.

2.2.4 Ground Offset Considerations

With regards to ground offset in the case of resistive sensing, we need to take certain measures in order to obtain battery voltages as accurately as possible (see Figure 2.2-11).
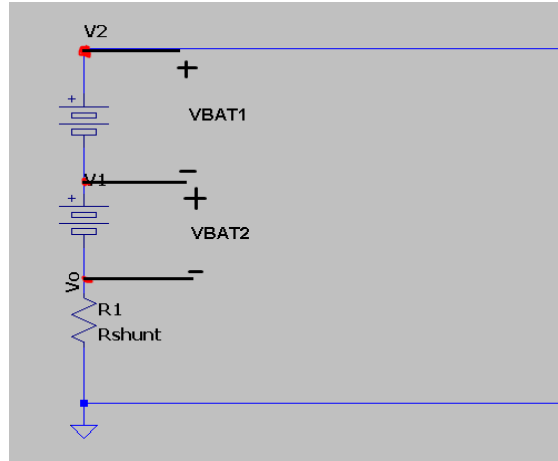
Figure 2.2-11 : Voltage measurement issue depicted.

We will need a mechanism to nullify the effect of the voltage drop across Rshunt. In other words, the battery voltages need to be obtained in the following manner:

$$VBAT1 = V1 - Vo \qquad\qquad (15.2.2)$$

$$VBAT2 = V2 - VBAT1 \qquad\qquad (16.2.2)$$

Where VBAT2 and VBAT1 are the voltages of the upper and lower battery in Figure 2.2-11 respectively. The voltage dividers should be placed at node V1 and V2. While Vo is to be determined through the current and known resistor value. In addition, 12 gauge wire (4 mm² cross sectional area) was used between the negative terminal of BAT1 and Rshunt in order to avoid additional offset since it has a very low resistance. The rest of

the circuit (in series with the load) was constructed using 16 gauge wires (1.5mm² wires). We will refer to the voltage of the batteries as VBAT1 and VBAT2 for the rest of the report.

2.2.5 Voltage Measurements' Overall Design

We picked voltage dividers with an attenuation factor of 40 and 22 for the measuring VBAT1 and VBAT2 respectively; that has been done in order to limit those voltages to the 0.4V-0.6V range which is below the microcontroller's reference voltage (1.1V). The attenuation factors were also chosen in order to bias our signal in the middle of the ADC output characteristics which maximizes voltage measurement accuracy (see Figure 2.2-8).We get the total quantization error by multiplying equation 3.3.6 by the attenuation factors. We get a total quantization error of ±0.01V and ±5.75 mV for the VBAT1 measurement and the VBAT2 measurement respectively. Since we will be measuring the voltages of two 12V batteries in series (see 2.1 for battery specifications), the minimum voltage should be around $10V^3$ which means that it is possible to bias the input analog signal in the middle of the ADC output graph. In addition, 12 bits of resolution (at a voltage reference of approximately 1.1V) will lead to an error of $\pm$ 5.36 mV which is acceptable. This implies that the internal ESP32 ADCs are the best choice for our application. We use 10KΩ resistors in series with 260Ω resistors to obtain the necessary attenuation factor VBAT1, and 10KΩ in series with 470Ω for VBAT2. Since the voltage is affected by the ground offset which is caused by the increase in current, multiple voltage measurements were taken at multiple discharge rates. The INA219 was chosen as the current sensor for providing feedback for the active load since it is the most accurate one (see section 3.6). The overall circuit is shown in Figure 2.2-12.

---

[3] The minimum battery voltage for Lead-acid batteries is around 10V; however, as we will see later on, the terminal voltage can drop below that and can even reach the lower threshold of the ADC range. That means that the batteries have been over-discharged and need to be recharged.
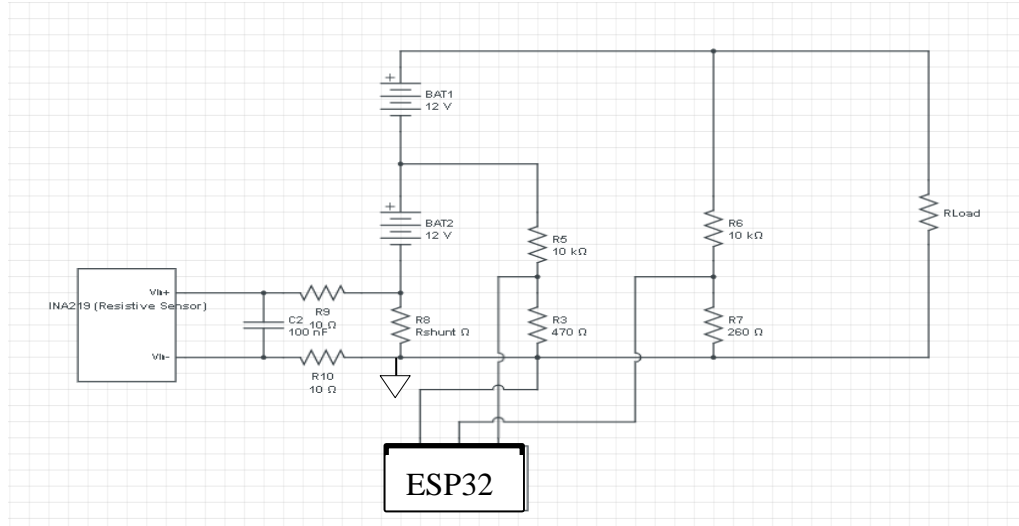
Figure 2.2-12 : Overall circuit for voltage measurements.

2.3 Current Measurements

Accurate current measurement is essential for a decent coulomb counting, hence a decent SOC estimation; in order to comfortably gauge the reliability of a current sensor, we have designed an active load consisting of an SFH154 avalanche rugged linear power MOSFET and an amplifier. The ESP32's DAC is used to control the gate voltage of the MOSFET to limit the current flow. A feedback loop is incorporated through whichever current sensor is picked (see Figure 2.3-1 and Figure 2.3-2).
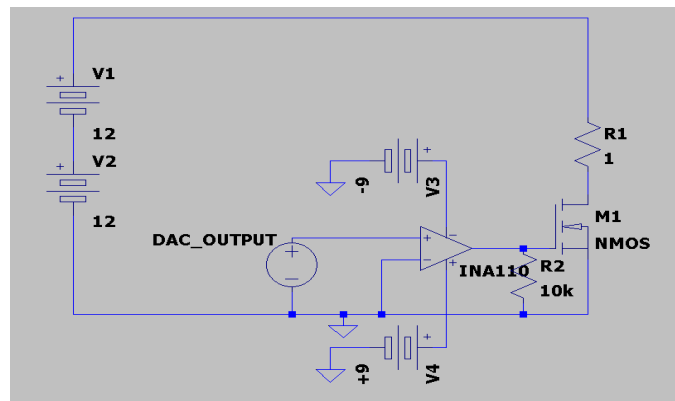
Figure 2.3-1 : Active load circuit.

Chapter 2. Solar Battery Monitoring Design
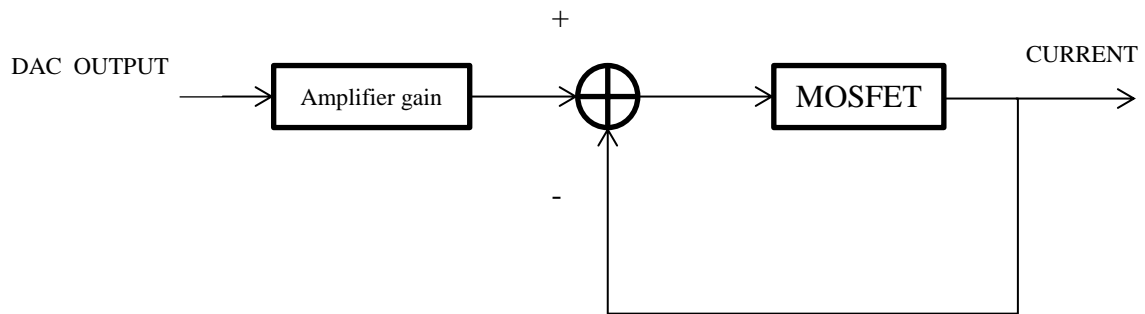
Figure 2.3-2 : Feedback loop for controlling the current draw.

The one ohm power resistor (R1) at the MOSFET's drain is a failsafe measure in case of an internal short as well as a power sink: it allows the MOSFET to pass more current while staying in its safe operating area. 12 Gauge wire was used from the source terminal to ground. Adequate thermal design should be considered before implementing this circuit.

2.3.1 Thermal Design

Our main goal is to be able to pass a maximum of 6A through the MOSFET without any damage to the hardware. That is because it is dangerous to discharge batteries with unknown current draw limitations beyond their rated capacity's value (ex. You should not discharge a 4Ah beyond 4A unless it is deemed safe by the manufacturer). After consulting the MOSFET's datasheet and finding out its thermal resistance we construct the following thermal circuit (see Figure 2.3-3):
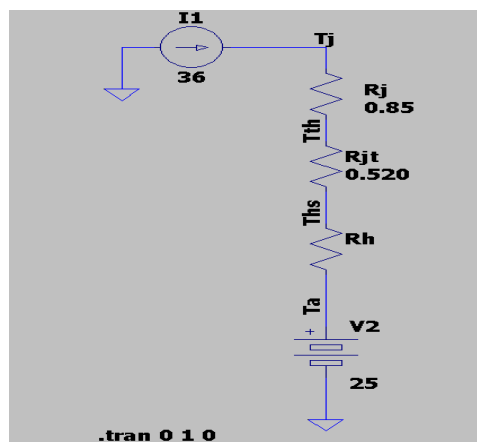
Figure 2.3-3 : Thermal circuit of the active load

Rj : the junction-to-case thermal resistance.
Rjt : the case-to-sink resistance (thermal paste resistance).
Rh : the heatsink thermal resistance
I1 : the dissipated power by the SFH154 at 6A which is 36W.
Tj: junction temperature (must not exceed 150C°)
Ths: heatsink temperature.
Tth: thermal paste temperature.
Ta: is the ambient temperature and varies from 25C° to 28C°.

We tested a Dual Core fan equipped CPU heatsink and measured its thermal resistance. In order to measure its internal resistance, we clamped the MOSFET to the heatsink using threaded bolts and a metallic sheet after applying thermal paste to reduce its thickness, and hence, enhance its thermal conductivity.

The thermal resistance of the heatsink is given by the formula.

$$Rh = \frac{Ths - Ta}{Q} \tag{17.2.3}$$

Where Q is the power dissipation which is given by:

$$Q = Vds \times I \tag{18.2.3}$$

Rh : the heatsink thermal resistance
 I:Current flowing through the load.
Ths: heatsink temperature..
Ta: is the ambient temperature and varies from 25C° to 28C°.
Q: is the power dissipation
Vds: is the drain to source voltage

In order to figure out the value of the maximum allowed thermal resistance of the heatsink, we used equation 19.2.3:

$$Rh(\text{max}) = \frac{Tj(\text{max}) - Ta}{Q} - Rjt - Rj \tag{19.2.3}$$

We found that a heatsink of thermal resistance Rh(max)=1.68 C°/W or less is required to keep the MOSFET junction below 150C° at 6A where Rh(max) is the maximum thermal resistance allowed for the heatsink and Tj(max) is the maximum junction temperature 150C°.

2.3.2 Comparing Current Sensors

In order to pick a current sensor, knowing its theoretical accuracy is not enough; we need to also evaluate its advantages and disadvantages and confirm its accuracy experimentally.

Chapter 2. Solar Battery Monitoring Design

Since we will be measuring both discharge and charging current, the current sensors need to be bidirectional.

2.3.2.1 INA219

The INA219 is a resistive sensor consisting of a Delta-sigma ADC and a PGA; it works on the principle of oversampling and decimation. It is advertised to have a total error of $\pm 0.5\%$. Its advantages consist of:

- Having the second highest advertised accuracy of the current sensors I am going to present next.

- No conditioning circuit is needed for it to operate with a microcontroller. It is equipped with its own I2C Delta-sigma ADC and PGA which allows us to avoid accuracy loss caused by another digital conversion stage, as well as making the design simpler and cheaper.

- While it has some attractive advantages, it also has a multitude of disadvantages which mainly consist of:

- A maximum common mode voltage tolerance of 26V: since we have 24V on our high-side, it is dangerous to place our sensor there; therefore, the current will have to be placed on the low side, which means that there will be ground offset caused by the sense resistor near ground.

-The need for a low-pass filter as per datasheet instructions to avoid harmonics at the 0.5 Mhz range.

2.3.2.2 LA 100P

The LA 100P is a Hall effect compensated DC CT. It is advertised to have a total error of $\pm 0.45\%$ under ideal conditions (± 15V supply, T=25C°). Its advantages are:

- It is galvanically isolated from the load line. (the wire goes inside the loop without having to place the sensor in series with the load).It has the highest advertised accuracy of the sensors presented in this report (under ideal conditions).Its disadvantages are numerous:

- The need for an analog to digital conversion stage (ADC) in order to interpret the output.

- The need for a conditioning circuit. A sense resistor of 20 ohms needs to be placed on its output in order to convert the current into voltage which further increases error.

- Its high accuracy is highly subject to variation in temperature and supply voltage. It is required to implement a magnetic offset canceling mechanism before the measurements.

- It is the most expensive option of the three solutions.

2.3.2.3 ACS758

The ACS758 is a bidirectional Hall effect sensor. It is advertised to have a total error of ±1.2%. Its only advantage compared to its other counterparts (mainly the INA219) is the ability to be placed on the high side. Its disadvantages include but are not limited to:

- Having the highest total error of the three current sensors.

- Its error is likely to increase with other parameter variations such as temperature.

- The need for an analog to digital conversion stage.

- The need for a conditioning circuit.

Despite being a Hall effect sensor, the ACS758 needs to be placed in series with the load: That is because it does not have an incorporated magnetic core to direct the magnetic flux into the Hall effect sensor as we have seen in Figure 1.2-2, but instead, a current conductor of 100 micro-ohms and a magnetic concentrator as shown below.
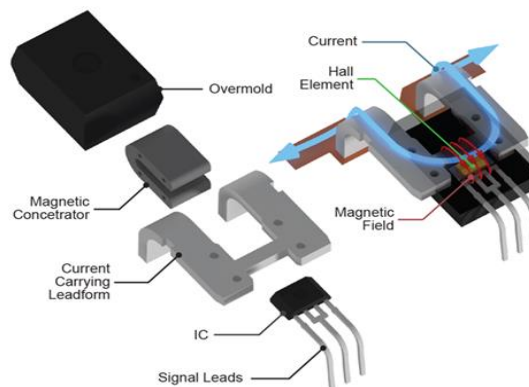
Figure 2.3-4 : Hall effect sensor structure [18].

Chapter 2. Solar Battery Monitoring Design

The reason behind using magnetic concentrators over magnetic cores is being able to shrink the sensor's size for high-density PCB design [18]. This also makes the sensor cheaper since high current ferrite cores are expensive.

2.3.3 Current Sensor Testing Circuit

We used the circuit in Figure 2.3-5 for testing the current accuracy for all the sensors, with the exception of adding an ADS1115 for the LA 100P, and ACS758. After determining the best sensor through our results, we keep the same circuit and use that sensor for providing feedback to the active load while doing our voltage measurement tests.
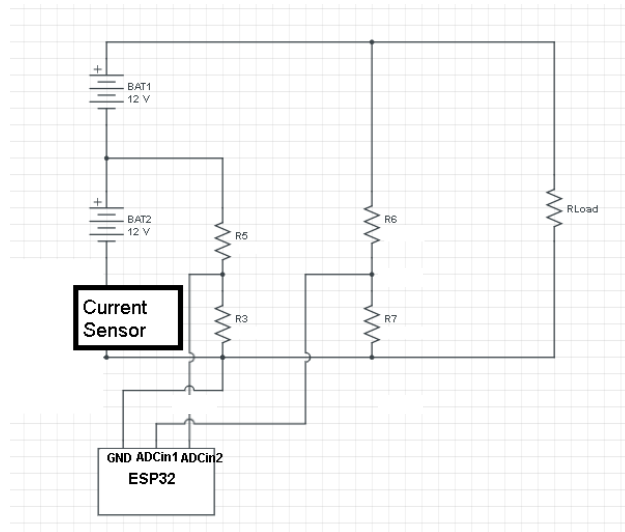
Figure 2.3-5 : Overall circuit for current sensor testing.

2.4 The SOC Estimation Algorithm

As we have previously mentioned in 1.3.3, combining OCV method and coulomb counting yields the best results for SOC estimation [14]. We also know that it is necessary to account for the Peukert effect and coulombic efficiency for an ideal estimation. Figure 2.4-1 shows how the overall algorithm should be implemented on the ESP32. The entire code was written in C language through the ESP-IDF development framework. Preprocessor statements were used in order to conveniently switch from one current sensor to another for testing purposes. MeasureVolts() is the function responsible for obtaining ADC samples and multisampling. CurrentRead() is the function which handles I2C communication between the ESP32 and the ADS1115 (for the ACS758 and LA 100P) or the ESP32 and the INA219. Its source code changes depending on which current sensor we

pick in our preprocessor statements. We then map the initial SOC ($SOC(t_0)$) after measuring voltage from the discharge curve (which is approximated linearly). Since we will use coulombic efficiency for charging, and Peukert compensation for discharging, we have to know whether the battery is being charged or discharged (if the change in SOC ΔSOC is positive or negative). To obtain that information, we integrate the current Ieff1 since it is just the current I(t) divided by the nominal capacity times the coulombic efficiency which is considered constant during one integration period. We then proceed to re-evaluate ΔSOC depending on whether its previously obtained value was positive or negative: If it was positive then we keep the value of ΔSOC, if not, then we proceed with Peukert compensation (we integrate I(t)/Ca the actual capacity). We then measure the voltage once more to check if the batteries have reached the full charge terminal voltage (Vfull) or the full discharge terminal voltage (Vempty). If that is the case, we calibrate the integral by mapping the SOC from the discharge curve (SOC=0% if V=Vempty, SOC=100% if V=Vfull). We then upload all of our data (voltage, current , SOC) into the cloud.
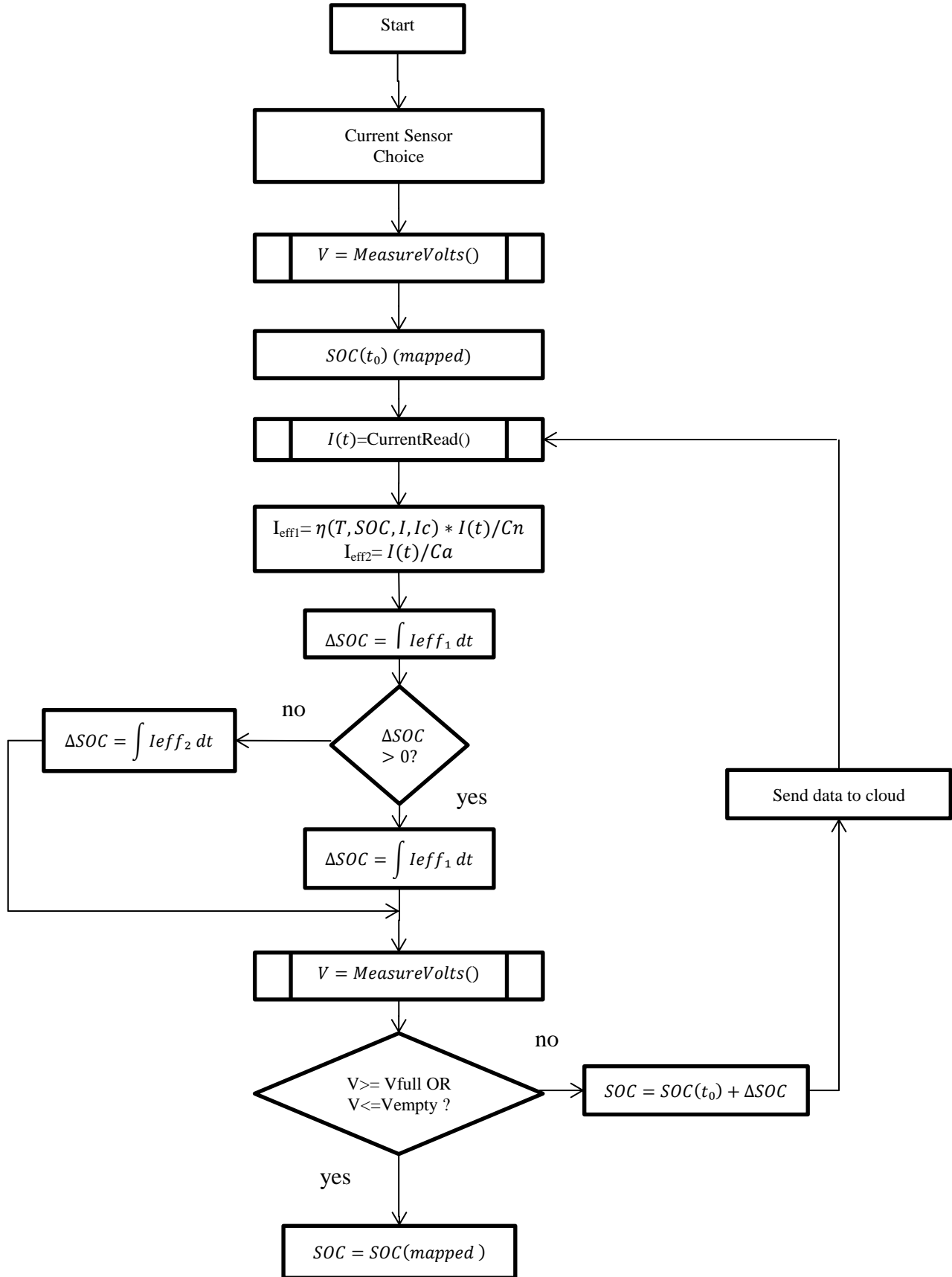
Figure 2.4-1 : Flow chart of the overall algorithm for obtaining voltage, current and SOC.

Chapter 2. Solar Battery Monitoring Design

2.5 Calculations for the Algorithm

In order to check the accuracy of our SOC estimation algorithm, two theoretical batteries with the following specs were considered. This allows us to also test the accuracy of the Peukert compensation and Coulomb counting:

I=0.928A

BAT1: C1=1Ah, R1=20h, pc1=1.5

BAT2: C2=1Ah, R2=20h, pc2=1.2

C1,2: nominal capacity of BAT1 and BAT2 respectively.

R1,2: discharge rate of BAT1 and BAT2 respectively.

pc1,2: peukert exponent of BAT1 and BAT2 respectively.

I: discharge current.

Using equation 7.1.3 we get :

Cp1=0.223Ah,Cp2=0.548Ah

Using equation 8.1.3, Cp1, and Cp2 we get :

Ca1=0.245Ah, Ca2=0.588Ah.

Ca1,2: actual capacity of BAT1 and BAT2 at the current I respectively.

 This in turn gives us a total discharge time of:

T1=0.25h, T2=0.6h.

Where T1 and T2 are the discharge times for BAT1 and BAT2 respectively.

Chapter 3. Implementation and Results

A multitude of tests have been conducted in order to find the appropriate data (accuracy, and reliability) for deducing the best choice of hardware and algorithms for voltage, current, and state of charge measurements.

3.1 Implementation

3.2 The Thermal Resistance Measurement Circuit

Our main objectives are implementing the aforementioned circuits and obtaining the accuracy results. Figure 3.2-1 shows a picture of the heatsink resistance measurement setup (multi-meter showing heatsink temperature). We know that our CPU heatsink is designed to dissipate significant amount of power since was designed for cooling a Dual core CPU which can generate up to 65W of heat power. We set the DAC to limit the current at specific values in order to control the power dissipated as heat, then, we measure the ambient temperature and Vds using the aforementioned multi-meter. We let the heat propagate along the heatsink for 6 minutes before measuring its temperature.
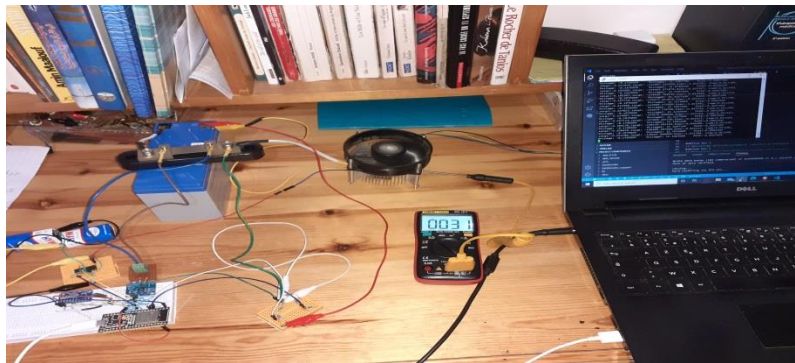
Figure 3.2-1 : Picture showcasing the Heatsink thermal resistance measurement circuit

3.3 The Current Sensor Testing Circuits

Similarly, we discharge the batteries at various currents to see the current sensors' actual output error. In every test, the multi-meter was placed in series with the load in order to obtain the actual current values. For the LA 100P and ACS758, an ADS1115 was used in order to minimize analog to digital conversion errors and to measure current bi-directionally as mentioned in 2.2.3. A magnetic offset cancellation algorithm consisting of measuring the no load output of these sensors and subtracting it from the measurements

has been implemented. Figure 3.3-1 and Figure 3.3-2 showcase the connection of the LA 100P and the ACS758 to the ADS1115.
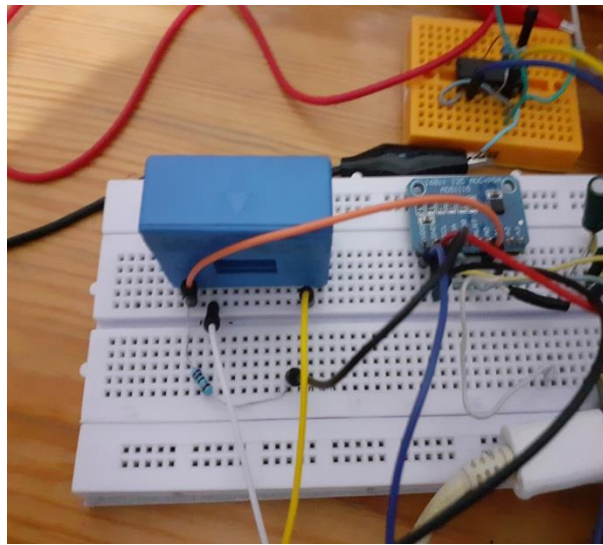
Figure 3.3-1 : LA 100P output measured through ADS1115
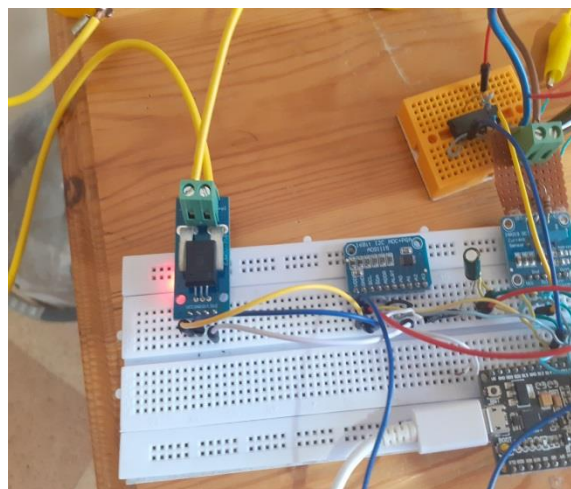
Figure 3.3-2 : ACS758 output measured through ADS1115

The capacitor shown in the figure is only there to compensate for a board defect in the ESP32 used in these tests. This defect consists of not being able to flash codes properly and has no effect on the chip's performance. For the INA219, a low-pass filter is placed at its input stage in order to reduce the harmonics. The harmonics are caused by the analog to digital conversion, hence why they are so close to the operating frequency of the ADC (1Mhz). As per datasheet instructions, a 0.1μF ceramic capacitor and two 10 ohm resistors at each side of the input (Vin+ and Vin-) were used (cut off frequency of 80Khz<500Khz). Figure 3.3-3 and Figure 3.3-4 show the effect of this low-pass filter on the peak to peak noise value while both inputs are grounded (see upper right corner).

Figure 3.3-3: Average noise value without the low pass filter
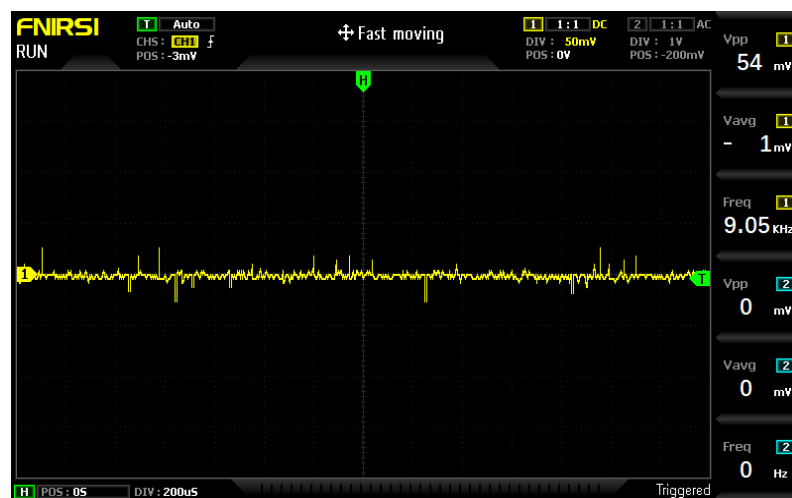
Figure 3.3-4 : Average noise value with the low pass filter

As we can see, the peak to peak value of noise (upper left corner of Figure 3.3-3 and Figure 3.3-4) is about three times greater without the low-pass filter (Vpp=54mV in Figure 3.3-3 and Vpp=151mV in Figure 3.3-4).

3.4 The Voltage Accuracy Testing

For the voltage measurements, we use an alligator wire to firmly connect the shunt resistor to the ESP32 ground through the voltage divider grounds. This is done in order to eliminate ground offset from our measurements. The oversampling and averaging is done through a simple while loop

3.5 The Peukert/Coulomb Counting Compensation Algorithm

We upload the code of the voltage, current, and SOC estimation represented by Figure 2.4-1 into our microcontroller after defining the value of the INA219 as 1 (meaning the code for the INA219 will be compiled) and plugging the values of Cp1,2 and pc1,2 into

Chapter 3. Implementation and Results

their variable assignments. We kept the exact same circuit as the one used for voltage measurements (see Figure 2.2-12).

3.6 Results

3.6.1 Heatsink Thermal resistance

Using the formulae 17.2.3 and 18.2.3, we filled Table 3.6-1 with the values of Q the power dissipation, and Rh the heatsink thermal resistance. We also calculated the average value of Rh.

Table 3.6-1 : Heatsink resistance measurements.

I(A)	Q(W)	Ta	Th	Rh
0	5.72	26	27	0.175
1	10.68	26	29	0.281
3	16.89	27	30	0.177

Rh(average)= 0.211 C°/W < Rh(max) (see 19.2.3).

This heatsink is a suitable choice for our design.

3.6.2 Current Measurements

We will be discussing the results of accuracy for all sensors. I(meas) represents the current measured with a multi-meter, while I(sens) is the current measured by the sensor for every results table in this section.

3.6.2.1 LA 100P Results

Since a ±12V supply was used for this test, as per datasheet info, the error should be around ±0.7% but since we are using a ±0.1% error resistor for the output current sensing, the overall error becomes ±0.8%. After doing the tests, Table 3.6-2 was obtained.

Table 3.6-2 : Error measurements for the LA 100P.

Imeas(A)	Isens(A)	Error (%)	Average Error(%)
4.66	4.63	0.64	
1.4	1.42	-1.42	
0.4	0.41	-2.5	
1.3	1.32	-1.53	-1.20

Chapter 3. Implementation and Results

The error value obtained experimentally is -1.2%. As expected, the sense resistor we used definitely does add error into our measurements, which is why the experimental value of error is closer to our estimated overall error than the datasheet specified error value.

3.6.3 ACS758 Results

The expected error of the ACS758 should be around ±1.2% as per datasheet info. Table 3.6-3 was obtained after our measurements.

Table 3.6-3 : Error measurements for the ACS758.

Imeas(A)	Isens(A)	Error (%)	Average Error(%)
0.359	0.575	-60.16	
0.259	0.3	-15.83	
1.99	2.99	-50.25	
4.1	4.91	-19.75	-36.50

Surprisingly enough, this sensor was remarkably inaccurate (36%) and the error wasn't caused by a constant offset that can be nullified as can be seen on the table. The ambient temperature during the measurements was 26 C° while conducting the discharge tests and is close to the ideal operating temperature 25 C°. The current sensor used in this experiment is most certainly a counterfeit chip.

3.6.3.1 INA219 Results

The expected error should be around ±0.5% since there is no additional error in our system besides the harmonics, which we cannot perfectly predict their impact theoretically. Experimentation provided us with Table 3.6-4.

Table 3.6-4 : Error measurement for the INA219.

Imeas(A)	Isens(A)	Error (%)	Average Error(%)
0.365	0.361	1.09	
0.259	0.258	0.38	
1.36	1.35	0.73	
4.35	4.32	0.68	0.72

The total error obtained experimentally is 0.72% which is close to the value in the datasheet. From the data above we can safely say that the INA219 is the best choice for our application and it satisfies our needs (1% accuracy).

Chapter 3. Implementation and Results

3.6.4 Voltage Measurements

The expected error should be around ±1% (caused by the resistors of the voltage divider) for VBAT1 (see equation 15) and around ±2.2% for VBAT2 (caused by the resistors, the ground offset measurement accuracy of the INA219, and VBAT1 measurement). Table 3.6-5 was obtained after conducting the aforementioned voltage accuracy tests. VBAT1 and VBAT2 are the same voltages mentioned in 2.2.4 and obtained through the ADCs; on the other hand, VBAT1a and VBAT2a are their multi-meter measured counterparts.

Table 3.6-5 : Voltage measurement error.

I(A)	VBAT1(V)	VBAT2(V)	VBAT1a(V)	VBAT2a(V)	error1(%)	error2(%)
0	12.33	12.88	12.36	12.82	0.24	-0.46
0.5	12.04	12.26	12.07	12.21	0.24	-0.40
1	11.911977	12.03	11.91	11.94	-0.016	-0.75
3	11.33	11.08	11.5	11.01	1.47	-0.63

Error1(avg)=0.48%,Error2(avg)=0.57%

Error1(avg) is the average error for VBAT1 measurements while Error2(avg) is the average error for VBAT2.

As expected, the error is higher for VBAT2 than for VBAT1 because VBAT2 depends on VBAT1 (see Figure 2.2-11). Our system meets our design specifications (1% accuracy).

3.6.5 Algorithm Test for Determining SOC

We plugged the values Cp1, Cp2, pc1, and pc2 found in 2.4 into our algorithm and ran a current of 0.928A through our electronic load. We obtained the SOC curves and checked whether they match the calculations we have made in 2.5. BAT1 is supposed to reach 0% in 15 minutes while BAT2 will do that in 36 minutes. This will allow us to see how the Peukert effect affects battery SOC. We used Thingspeak for cloud storage since it stores time automatically. The calculations were explained in sections 1.3.4, 2.5, and in 0.

Chapter 3. Implementation and Results

Figure 3.6-1 : Peukert compensation results

From Figure 3.6-1 we see that BAT1 reaches 0% at 17 minutes (starting from 17:59 to 18:16) and BAT2 at 40 minutes. This is an acceptable error margin (-0.0928 Ah of error in an hour) considering the fluctuations of current of our electronic load seen on the upper left graph. This error will be reduced even further with OCV calibration.

Conclusion

The aim of this project was designing a voltage and current sensing circuit using the ESP32 microcontroller while using Coulomb counting and Peukert compensation to estimate SOC. The results of our tests showed us that we can achieve an accuracy of 0.7% for current measurements using the INA219. The ESP32's internal ADCs proved to be a reliable option, all the while being the cheapest and simplest one: a voltage accuracy of 0.48% and 0.57% for the first and second battery (which are in series) respectively was achieved using those internal ADCs. SOC estimation has proven to be reliable as well. This design does have some downsides however. For one, you cannot properly compensate for the Peukert effect and coulombic efficiency without having the necessary data to do so. In addition, this system only works reliably under a relatively constant temperature, which might not be achievable for solar batteries because of their placement and wire power loss considerations. Future work can be done in temperature compensation using temperature integrated-circuits and coulombic efficiency determination through a charge-discharge controller. Age compensation is also another area which this project can expand upon in order to truly maximize the useful life span of even a relatively old battery.

References

[1] D. S. Arar, "allaboutcircuits," EETech Media, 2019. [Online]. Available: https://www.allaboutcircuits.com. [Accessed 8 April 2022].

[2] Libre Texts, "Libre Texts," Libre Texts, 2020. [Online]. Available: https://chem.libretexts.org. [Accessed 6 6 2022].

[3] Espressif, "Esp-idf API Reference," 2022. [Online]. Available: https://docs.espressif.com/. [Accessed 7 April 2022].

[4] Microsemi(Actel), Microsemi(Actel), 2007. [Online]. Available: https://www.microsemi.com. [Accessed 7 April 2022].

[5] EFTON s.r.o, "efton," 2020. [Online]. Available: http://www.efton.sk/. [Accessed 14 April 2022].

[6] S. Ziegler, "Researchgate," 2008. [Online]. Available: https://www.researchgate.net/. [Accessed 15 April 2022].

[7] S. M. a. J. V. Georges El Bacha, "Allegromicro," Allegro MicroSystems, LLC, 2014. [Online]. Available: https://www.allegromicro.com. [Accessed 5 6 2022].

[8] LEM, "LEM," 2022. [Online]. Available: https://www.lem.com. [Accessed 27 April 2022].

[9] C. Mathas, "Digi-Key," 2012. [Online]. Available: https://www.digikey.com. [Accessed 27 April 2022].

[10] W.-Y. Chang, "The State of Charge Estimating Methods for Battery: A Review," *International Scholarly Research Notices,* vol. 2013, no. 953792, p. 7, 2013.

[11] PowerTech Systems, "PowerTech Systems," PowerTech Systems, 2022. [Online]. Available: https://www.powertechsystems.eu. [Accessed 5 6 2022].

[12] J. M. a. K. B. Jiale Xie, "Enhanced Coulomb Counting Method for State-of-Charge Estimation of Lithium-ion Batteries based on Peukert's Law and Coulombic Efficiency," *Journal of Power Electronics,* vol. 18, no. 3, p. 13, 2018.

[13] Y. K. A.G. Stefanopoulou, Rechargeable Lithium Batteries, Cambridge: Woodhead Publishing Series, 2015.

[14] D. Andrea, "Li-ion BMS," Davide Andrea, 2009. [Online]. Available: http://liionbms.com/. [Accessed 4 May 2022].

[15] Power-Sonic, "Power-Sonic," 2011. [Online]. Available: https://www.power-sonic.com/.

References

[Accessed 4 May 2022].

[16] SmartGauge Electronics, "SmartGauge," SmartGauge Electronics, 2008. [Online]. Available:
http://www.smartgauge.co.uk/peukert2.html. [Accessed 4 May 2022].

[17] Victron Energy, "Victron Energy," Victron Energy, 2022. [Online]. Available:
https://www.victronenergy.com/. [Accessed 5 May 2022].

[18] G. Knuepffer, "Rethink What Is Possible for PCB Current Sensing," *Elektronik Industrie,* p. 1,
2020.

[19] ShawnHymel, "DigiKey," Digi-Key Electronics, 2022. [Online]. Available:
https://www.digikey.com. [Accessed 8 April 2022].

Appendix

A. *Programs used for this project*

   https://github.com/AHZ456/BatteryM

B. *Thingspeak library*

   https://github.com/dahmadjid/ThingSpeak-idf

C. *Derivation of equation 8.1.3*

We plug the nominal values in equation 7.1.3 to get the value of Cp since it is constant for any given current.

$$Cp = Cn(In)^{pc-1} \qquad\qquad (20.1.3)$$

Where Cn is the nominal capacity, and In is the nominal current such that:

$$In = \frac{Cn}{tn} \qquad\qquad (21.1.3)$$

Where tn is the duration of discharge at the nominal current. We then proceed to use Cp to obtain the actual capacity Ca. From 7.1.3 we get t in terms of Cp, I and pc.

$$Ca = I \cdot t = I \cdot \frac{Cp}{I^{pc}} \qquad\qquad (22.1.3)$$

We get then obtain Eq 8.1.3.

D. *Finding the value of the thermal resistance of the thermal paste*

The silicon-based thermal grease used is advertised to have a thermal conductivity of 0.6 W/m·C° we use the following formula to obtain the thermal resistance.

$$Rjt = \frac{t}{A \cdot k} \qquad\qquad (23.2.3)$$

Where k is the thermal conductivity, t is the thickness of the layer of thermal paste which was assumed to be 0.1 mm (loose pressure clamping), and A is the surface area of the transistor in contact with the heatsink.
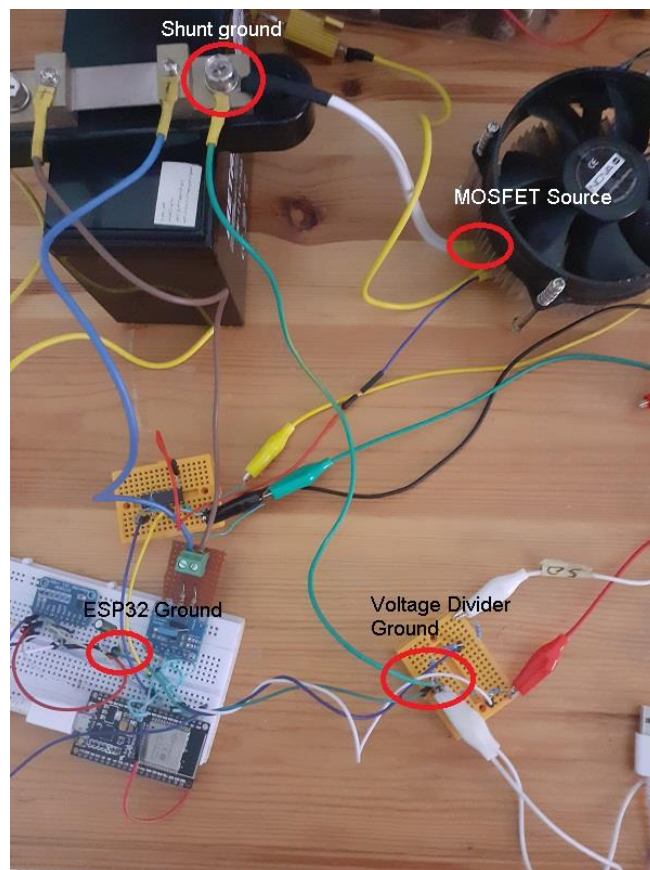
E. *Showing how the connection in 3.4 is made*

Appendix

Figure 3.6-2 : Ground connection.